Kinetics of CO/CO2 and H2/H2O reactions at Ni-based and ceria-based solid-oxide-cell electrodes

Graves, Christopher R.; Chatzichristodoulou, Christodoulos; Mogensen, Mogens Bjerg

Published in:
Faraday Discussions

Link to article, DOI:
10.1039/c5fd00048c

Publication date:
2015

Document Version
Peer reviewed version

Faraday Discussions
Cite this: DOI: 10.1039/c5fd00048c

PAPER

Kinetics of CO/CO_2 and H_2/H_2O reactions at Ni-based and ceria-based solid-oxide-cell electrodes

Christopher Graves,* Christodoulos Chatzichristodoulou and Mogens B. Mogensen

Received 1st May 2015, Accepted 6th May 2015
DOI: 10.1039/c5fd00048c

The solid oxide electrochemical cell (SOC) is an energy conversion technology that can be operated reversibly, to efficiently convert chemical fuels to electricity (fuel cell mode) as well as to store electricity as chemical fuels (electrolysis mode). The SOC fuel-electrode carries out the electrochemical reactions $CO_2 + 2e^- \leftrightarrow CO + O^{2-}$ and $H_2O + 2e^- \leftrightarrow H_2 + O^{2-}$, for which the electrocatalytic activities of different electrodes differ considerably. The relative activities in CO/CO_2 and H_2/H_2O and the nature of the differences are not well studied, even for the most common fuel-electrode material, a composite of nickel and yttria/scandia stabilized zirconia (Ni–SZ). Ni–SZ is known to be more active for H_2/H_2O than for CO/CO_2 reactions, but the reported relative activity varies widely. Here we compare AC impedance and DC current–overpotential data measured in the two gas environments for several different electrodes comprised of Ni–SZ, Gd-doped CeO_2 (CGO), and CGO nanoparticles coating Nb-doped $SrTiO_3$ backbones (CGOn/STN). 2D model and 3D porous electrode geometries are employed to investigate the influence of microstructure, gas diffusion and impurities present at reaction sites.

Comparing model and porous Ni–SZ electrodes, the ratio of electrode polarization resistance in CO/CO_2 *vs.* H_2/H_2O decreases from 33 to 2. Experiments and modelling suggest that the ratio decreases due to a lower concentration of impurities blocking the three phase boundary and due to the nature of the reaction zone extension into the porous electrode thickness. Besides showing higher activity for H_2/H_2O reactions than CO/CO_2 reactions, the Ni/SZ interface is more active for oxidation than reduction. On the other hand, we find the opposite behaviour in both cases for CGOn/STN model electrodes, reporting for the first time a higher electrocatalytic activity of CGO nanoparticles for CO/CO_2 than for H_2/H_2O reactions in the absence of gas diffusion limitations. We propose that enhanced surface reduction at the CGOn/gas two phase boundary in CO/CO_2 and in cathodic polarization can explain why the highest reaction rate is obtained for CO_2 electrolysis. For all materials investigated, large differences

Department of Energy Conversion and Storage, Technical University of Denmark, Risø Campus, Frederiksborgvej 399, DK-4000 Roskilde, Denmark. E-mail: cgra@dtu.dk

observed between model electrode kinetics and porous electrode kinetics are modelled and discussed.

Introduction

The growing need for efficient and affordable production and storage of electricity currently drives the development of electrochemical energy conversion technologies. The solid oxide electrochemical cell (SOC) is a promising candidate that could play a key role in the transition to sustainable energy because SOCs can both store renewable electricity as fuels (electrolysis mode) as well as convert fuels to electricity (fuel cell mode), with high efficiency and high reaction rates in both modes.[1–4] Furthermore, SOCs can operate with carbonaceous feedstocks (hydrocarbons, CO, CO_2, *etc.*)[5–8]

A good physical and chemical understanding of the electrochemical reactions (ERs) that occur in the fuel-electrode, $CO_2 + 2e^- \leftrightarrow CO + O^{2-}$ and $H_2O + 2e^- \leftrightarrow H_2 + O^{2-}$, is crucial for addressing performance and lifetime limiting factors as well as for designing new improved electrodes. The reactions take place either at the 3-phase boundary (3PB) between the gas, O^{2-} conductor and e^- conductor, or at the 2-phase boundary (2PB) between the gas and the surface of a mixed ionic and electronic conducting (MIEC) solid, depending on the electrode materials. The conventional fuel-electrode is a 3PB-based, three-dimensional porous composite of Ni and yttria or scandia-stabilized zirconia (Ni–SZ, referring to either one) that exhibits high electrochemical activity but is often a major source of performance loss during long-term operation in both fuel cell and electrolysis modes due to 3PB poisoning, Ni mobility, carbon deposition, and other degradation mechanisms.[9–14]

Alternative electrodes comprised of MIEC materials show great promise with respect to avoiding these issues.[15,16] Acceptor-doped ceria is a well-known MIEC solid when exposed to a reducing environment and it exhibits high activity for the H_2/H_2O reaction when applied as an electrode.[17–20] Considerable effort has gone into understanding and modelling the reaction kinetics and mechanisms for the H_2/H_2O and CO/CO_2 reactions, especially for Ni–SZ electrodes,[21–25] but also more recently for ceria-based electrodes.[16,26–28]

However, relative activities for the CO/CO_2 and H_2/H_2O reactions are not well studied, even for conventional Ni–SZ electrodes. Ni–SZ is known to be more active for H_2/H_2O than for CO/CO_2 reactions, but the relative activity varies widely,[23] apparently depending on the electrode microstructure, geometry, and purity of materials and gas supplies. Here we compare AC impedance and DC current–overpotential data measured in the two gas environments for several different electrodes comprised of Ni/SZ, Gd-doped CeO_2 (CGO), and CGO nanoparticles coating Nb-doped $SrTiO_3$ backbones (CGOn/STN). The aim is to better understand the nature of the electrocatalytic activities observed for different electrode materials and geometries, which vary considerably for these two reactions.

Model electrodes are advantageous in that they provide a more well-defined, usually 2-dimensional, interface and corresponding ER zone compared with complex 3-dimensional porous electrode structures. However, the small interface in a large system is more susceptible to contamination by segregation of material from the electrode itself or from other solid or gaseous sources, which can make it

ART ■ C5FD00048C

a poor representation of the actual interface that the model electrode aims to investigate in a realistic technological electrode. It is therefore worthwhile trying to study both model and porous electrodes together to obtain the most useful information, which we attempt here in order to investigate the influence of microstructure, gas diffusion and impurities present at reaction sites.

Experimental

Several types of electrochemical cells were fabricated and subjected to electrochemical characterization, as illustrated in Fig. 1. Regarding notation, we adopt Ni–SZ to indicate a composite porous electrode and Ni/SZ to indicate an interface of Ni and SZ (as in a model electrode).

Cells with a Ni metal wire electrode contacting the polished surface of a $Y_{0.16}Zr_{0.84}O_2$ (YSZ) electrolyte pellet with a porous Pt counter electrode (prepared by sintering Pt paste) were assembled and tested in a single-atmosphere custom

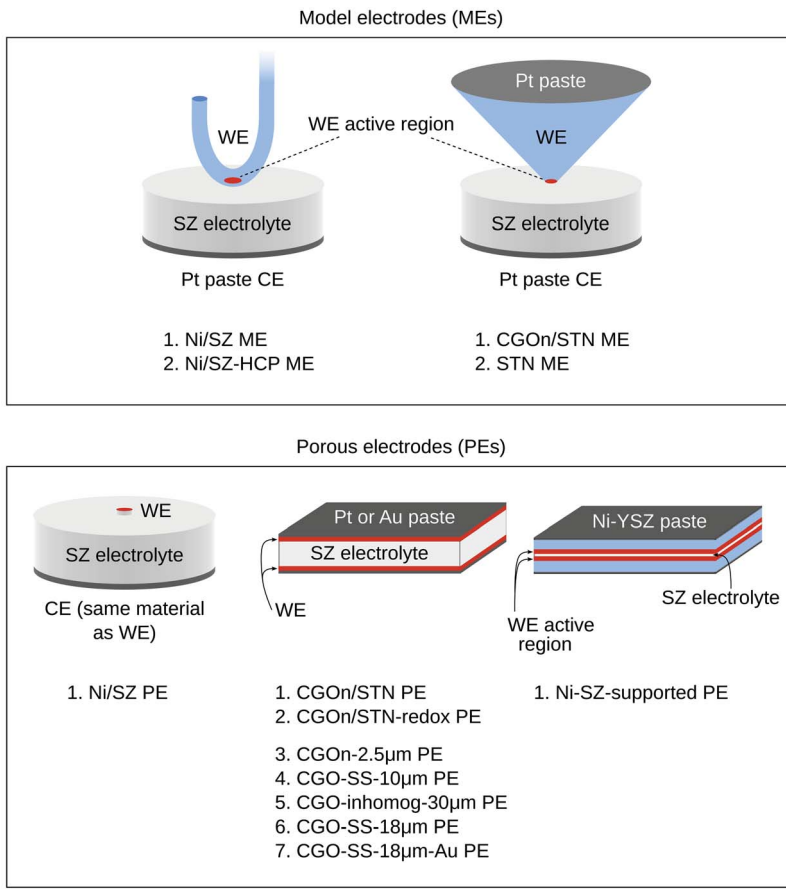

Fig. 1 Illustration of the different electrode geometries employed (WE = working electrode; CE = counter electrode) and list of electrode materials characterized (abbreviations are defined in the "Results and discussions" section).

ART ■ C5FD00048C

test rig, as described in ref. 29 and 30. A pseudo-three-electrode set-up was used, with the relatively large counter electrode expected to contribute negligible resistance and therefore serving as reference electrode. These types of model electrodes have a well-defined 3PB which can be examined by microscopy before and after testing. The wires were 0.5 mm in diameter and 99.999% purity. The wires were cut and bent approximately 1 cm from the end, to form a "J" shape, with the bottom of the "J" contacting the YSZ surface. The wires were annealed in a reducing atmosphere (pH_2/pN_2 = 0.09/0.91 atm). Each wire electrode was inserted into an alumina tube which held it in place and applied pressure downwards from a weight of 200 g attached above. The test rig was heated to an initial temperature of 1000 °C in pH_2/pN_2 = 0.09/0.91 atm which was then switched to pH_2/pH_2O = 0.97/0.03 atm, and electrochemical impedance spectra (EIS) were measured near open-circuit continuously for at least 10 hours until the interface stabilized. More extensive H_2/H_2O and CO/CO_2 gas variations were then tested. EIS were measured near open-circuit, from ~1 MHz to 0.1 Hz with 12 measurement points per decade, with an AC RMS amplitude of 30 mV, using a Gamry Reference 600 potentiostat, which was also used for DC polarization measurements at 1–10 mV s^{-1} between −300 mV and +300 mV overvoltage. The cell was wired such that anodic polarization corresponded to electrochemical oxidation of H_2 or CO (fuel-cell mode) at the working electrode, whereas cathodic polarization led the working electrode to carry out electrochemical reduction (electrolysis mode). Electrode current–overpotential curves were obtained by correcting the cell current–overvoltage curves for the ohmic resistance, which was measured by EIS.

High cathodic polarization (HCP) treatment was performed on some of the model Ni/YSZ electrodes. First, the gas atmosphere was set to dry H_2, reaching an oxygen sensor value of −1370 mV *vs.* air at 850 °C ($pO_2 < 10^{-24}$ atm). Then, the following potential sweeps were performed at a 20 mV s^{-1} scan rate: 0 to −500 mV, 0 to −1000 mV and 0 to −1500 mV. Upon reaching each cathodic voltage, EIS were also measured under that voltage. Finally, EIS were measured again near open-circuit after the HCP treatment.

Symmetrical cells with thin 5–10 μm YSZ electrolytes sandwiched by 10–15 μm thick porous Ni–YSZ active layers and 300 μm thick porous Ni–YSZ support layers were prepared by tape-casting and lamination. The cells can be considered as two fuel-electrode-supported half cells made symmetrical. The cells are the same types as those reported in ref. 31 and 32, except that these do not contain scandium. The cells were reduced at 1000 °C in pH_2/pN_2 = 0.09/0.91 atm in a furnace. Then the cells were painted with Ni–YSZ current collector paste and mounted in the same test rig as used for the model electrodes. The cells were heated to 800 °C in pH_2/pN_2 = 0.09/0.91 atm and switched to pH_2/pH_2O = 0.97/0.03 atm before more extensive H_2/H_2O and CO/CO_2 gas variations were tested. EIS measurements were carried out at 650–800 °C using a Solartron 1260 with 30 mV RMS amplitude from 1 MHz to 0.1 Hz with 16 measurement points per decade.

A new pseudo-3-electrode cell geometry was used for DC measurements on porous Ni–ScYSZ electrodes. A small (1 mm diameter) porous working electrode was screen-printed atop a special-shaped thick ScYSZ electrolyte pellet (approximately a cylinder 3 mm tall and 9 mm in diameter) with a large counter electrode screen-printed on the bottom and comprised of the same material as the working electrode. This small working electrode (SWE) configuration resembles the model

ART ■ C5FD00048C

wire electrode configuration, but with a 3D porous working electrode. Like the model wire electrode, this geometry minimizes ohmic heating and gas diffusion resistance. Details of the cell design will be reported in a future publication. The electrode was characterized with a similar procedure as that used for the model wire electrodes, using a Gamry Reference 600 potentiostat.

Symmetrical cells were prepared with electrodes comprised of porous $Sr_{0.94}Ti_{0.9}Nb_{0.1}O_3$ (STN) backbones coated with $Ce_{0.8}Gd_{0.2}O_{1.9}$ by surfactant-assisted nitrate solution infiltration, on both sides of a YSZ electrolyte, as described in ref. 33. Pt paste was applied to both electrodes for current collection. The cells were mounted in between Pt meshes with weight applied, in the same test rig as above. The cells were heated to an initial temperature of 800 °C in $pH_2/pN_2 = 0.09/0.91$ atm and switched to $pH_2/pH_2O = 0.97/0.03$ atm before more extensive H_2/H_2O and CO/CO_2 gas variations were tested. EIS measurements were performed using a Solartron 1260 with similar settings as for the Ni–YSZ symmetrical cells. During redox cycles, N_2 was supplied for 30 minutes before supplying air, and N_2 was again supplied before supplying the reducing atmosphere again.

Cone-shaped electrodes comprised of STN were prepared by machining dense cylindrical STN pellets that had been sintered at 1400 °C in $pH_2/pN_2 = 0.09/0.91$ atm. The cone point (working electrode) was contacted to a smooth polished YSZ electrolyte pellet surface, with a much larger porous Pt counter electrode acting as a reference electrode (pseudo 3-electrode setup), as described previously for other oxide electrode materials.[34] The cell geometry was similar in principle to the model wire electrode cell described above. For some electrodes, a drop of the same $Ce_{0.8}Gd_{0.2}O_{1.9}$ solution that was used to infiltrate the porous STN backbones was placed at the tip of the cone before contacting the cone to the YSZ surface. The cells were heated to 850 °C in $pH_2/pN_2 = 0.09/0.91$ atm and switched to $pH_2/pH_2O = 0.97/0.03$ atm, and EIS were measured continuously for at least 10 hours until the interface stabilized. The electrodes were characterized with a similar procedure as that used for the model wire electrodes using a Gamry Reference 600 potentiostat.

Symmetrical cells with porous $Ce_{0.9}Gd_{0.1}O_{1.95}$ (CGO) electrodes were prepared by slurry spraying (SS) or screen-printing onto a sintered 200 μm thick YSZ electrolyte and sintering at 1200 °C, similar to in ref. 35 which used CGO electrolyte. For the screen-printed electrodes, due to poor dispersion in the ink, the CGO particles agglomerated, resulting in an inhomogeneous microstructure after sintering at 1200 °C. The electrodes were characterized with a similar procedure as that used for the STN-backbone symmetrical cells described above. For one SS cell, Au paste was used instead of Pt paste.

Symmetrical cells with nano-porous CGO electrodes were prepared by spin-coating a nitrate based precursor solution. The electrodes were only sintered *in situ* at 800 °C, which resulted in the nano-porous structure. More detail about the structure and electrochemistry of these highly active electrodes will be reported in a future publication. The electrodes were characterized with a similar procedure as that used for the STN-backbone symmetrical cells described above.

All EIS reported here were measured near open-circuit. The gas compositions of $pH_2/pH_2O = 0.5/0.5$ atm and $pCO/pCO_2 = 0.5/0.5$ atm (hereafter simply referred to as H_2/H_2O and CO/CO_2) were chosen as the basis for comparison for several reasons:

ART ■ C5FD00048C

• In current–overpotential curves, they provide an equal concentration of reactants for both anodic and cathodic polarization.

• Gas diffusion impedance is minimized.[36] For porous electrodes, several important gas diffusion impedance contributions have been identified for electrodes measured in this test set-up: diffusion in a stagnant gas layer above the porous electrode that arises solely from the test set-up,[36,32] diffusion through thick porous layers,[32] and Knudsen diffusion through nanoparticle-loaded structures with fine porosity.[37] The stagnant gas layer diffusion resistance has been found to contribute 5 and 30 mΩ cm^2 in $pH_2/pH_2O = 0.5/0.5$ atm and $pCO/pCO_2 = 0.5/0.5$ atm, respectively, in the present study and in previous reports.[32]

• The 50–50 gas compositions give a very similar pO_2 in the measurement temperature range 750–850 °C.

Measurements were carried out in H_2/H_2O and CO/CO_2 as close in time as possible while also allowing enough time to stabilize, to avoid interference from relaxation and degradation, especially for the 3PB-based Ni/SZ model electrodes.[38] The ranges of the current–overvoltage curves were kept below ±300 mV, since Ni oxidizes to NiO near +300 mV at the temperature and gas composition used – going to too high an anodic overvoltage led to hysteresis in the current–overvoltage curve due to Ni oxidation. Each symmetrical cell has an area of about 30 mm^2. At least two electrodes of each type were tested for reproducibility, except that only one cell was tested with Au paste instead of Pt paste for current collection, which will be discussed later.

All data analysis was carried out using the python-based Ravdav software.[39] EIS measurements were corrected for stray inductance using an automatic Kramers–Kronig procedure. The model electrodes were not normalized to 3PB length or contact area in this study because: in the Ni wire electrode case, after the HCP treatment the 3PB length was not well defined and due to coarsening during subsequent measurements it was not possible to take post-test measurements of the *in situ* 3PB formed by the HCP treatment; in the CGOn/STN model electrode case, the CGO nanoparticles at the interface formed *in situ* and were similarly not well enough defined for sensible normalization.

Results and discussions

Ni/stabilized-zirconia 3PB-based electrodes

To investigate the effects of electrode microstructure and 3PB morphology on the ER kinetics of the Ni/SZ/gas interface, several different Ni/SZ electrodes were employed, with either 2D or 3D 3PB geometries (illustrated in Fig. 1):

1. A Ni wire pressed down onto a polished YSZ surface, forming a 2D 3PB at the perimeter of the oval-shaped contact (hereafter referred to as the "Ni/SZ model electrode" or "Ni/SZ ME").

2. The same Ni wire contacting the YSZ surface after it had been subjected to HCP treatment, which forms a new nano-structured 3PB ("Ni/SZ-HCP model electrode").

3. A porous Ni–YSZ composite symmetrical cell with 300 μm thick porous Ni–YSZ support layers sandwiching the thin porous Ni–YSZ active layer and thin dense electrolyte ("Ni–SZ-supported porous electrode").

4. A small-sized porous Ni-ScYSZ composite working electrode in the pseudo-3-electrode "SWE" cell configuration ("Ni–SZ porous electrode").

ART ■ C5FD00048C

Impedance spectra measured on each of the electrodes are shown in Fig. 2a–d. All cells except the 3rd cell (Ni–SZ-supported porous electrode; symmetrical cell) could be polarized to obtain DC current–overpotential measurements, which are shown in Fig. 3a–c.

For all of these electrodes, the electrochemical activity for the H_2/H_2O reaction was higher than for the CO/CO_2 reaction, but the relative activity near open-circuit varied from a factor of 33 (Fig. 2a and 3c) to a factor of 2 (Fig. 2c and d and 3i) depending on the electrode. These ratios are in a similar range to those previously reported for various Ni/SZ electrodes.[23] Here we address the reasons for the large differences in relative activity.

Impedance spectroscopy

The EIS measured on the model Ni/YSZ electrode exhibited a skewed semicircle that grows smaller with increasing frequency in the complex–complex plane (Fig. 2a), which matches previously reported measurements in H_2/H_2O on similar Ni wires contacting YSZ or ScYSZ surfaces.[29,40–42] The ratio of R_p for CO/CO_2 *vs.* H_2/H_2O (hereafter "C : H R_p ratio") is 33. After the HCP treatment, the impedance has changed dramatically (Fig. 2b), similar to the changes observed in measurements in H_2/H_2O for a model Ni/ScYSZ electrode subjected to HCP treatment at lower

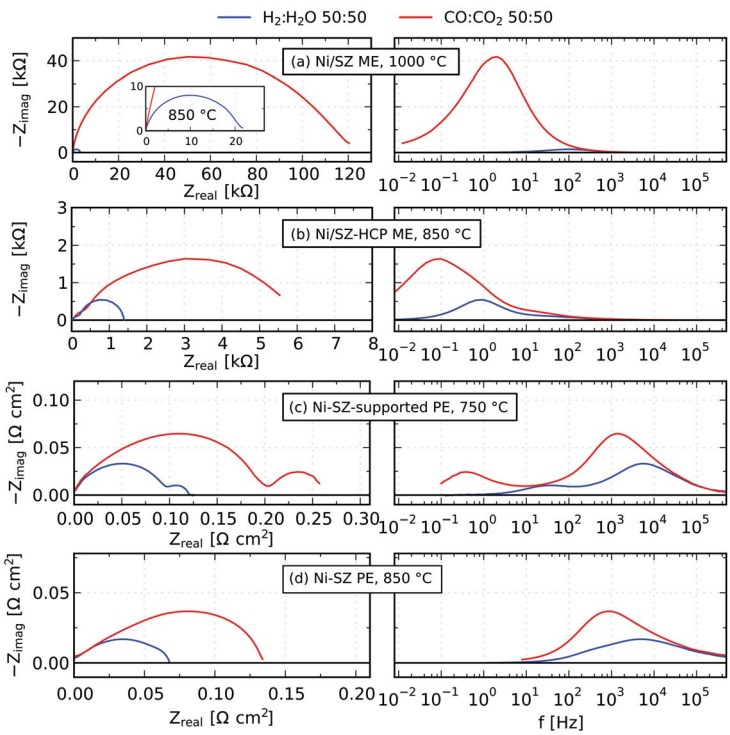

Fig. 2 Single-electrode impedance data measured on different Ni/SZ model (a and b) and porous (c and d) electrodes in 50 : 50 mixtures of H_2/H_2O and CO/CO_2. To obtain the single-electrode impedance, the ohmic resistance is subtracted for all data, and for (c) and (d) the symmetrical cell impedance is divided by 2.

ART ■ C5FD00048C

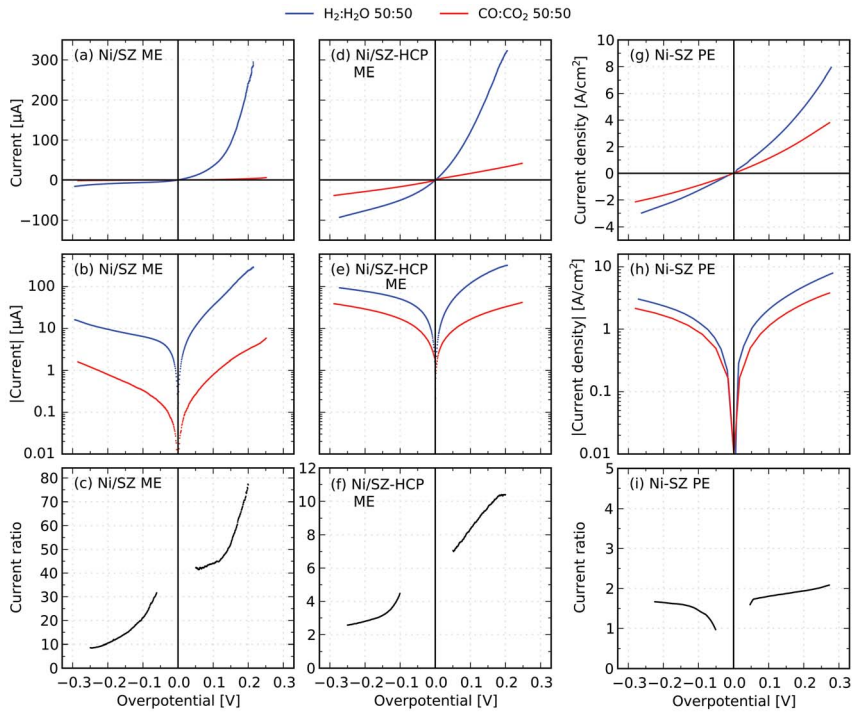

Fig. 3 Current–overpotential curves measured on different Ni–SZ model (a–f) and porous (g–i) electrodes in 50 : 50 mixtures of H_2/H_2O and CO/CO_2. Current ratio (c, f and i) is the ratio of the current measured in H_2/H_2O to that measured in CO/CO_2.

temperature.[42] The H_2/H_2O impedance is dominated by a single near-perfect semicircle and also shows a smaller high-frequency process. The CO/CO_2 impedance also displays a small high-frequency process and a possible multi-process peak dominating at lower frequencies. The C : H R_p ratio has decreased to ~4.5. Based on EIS measurements made on symmetrical cells with the Pt/YSZ counter electrode on both sides, the small high-frequency process appears to be the counter electrode,[29] which was negligible before the HCP treatment and became visible due to the decreased electrode R_p resulting from the HCP treatment.

The porous Ni–SZ electrodes gave a typical Gerischer-like porous electrode impedance response,[32,43,44] with skewed semicircles that lean the opposite way compared to the model Ni/YSZ electrode (Fig. 2c and d). The EIS of the Ni–SZ-supported porous electrode exhibits an additional low-frequency process (Fig. 2c), which was previously shown to be gas diffusion in the thick porous support layer.[32] The SWE Ni–ScYSZ electrode impedance has no such low-frequency process, illustrating that the gas diffusion resistance is minimized in this porous electrode geometry. For both electrodes, the C : H R_p ratio is 2, suggesting a confirmation of previous reports that the use of ScYSZ does not change the 3PB reaction mechanism compared with YSZ.[42]

It should be noted that although the presented EIS data was measured at different temperatures, the C : H R_p ratios are approximately the same throughout

ART ■ C5FD00048C

the measurement range due to the similar activation energies of the H_2/H_2O and CO/CO_2 reactions, as is evident from comparison with the current–overpotential curves which were all measured at 850 °C. The general shapes of the spectra are also very similar throughout the measurement range 750–1000 °C. The presented spectra were chosen for illustrative purposes. For example, the 1000 °C measurements are shown for the model Ni/SZ electrode because at lower temperature the CO/CO_2 impedance process goes to very low frequencies and therefore most measurements did not include the full arc. The inset shows the H_2/H_2O measurement at 850 °C, which has the same shape. Table 1 gives a summary of the EIS results for all of the model and porous Ni-based electrodes.

Current–overpotential curves

In agreement with the EIS results, at low current the current–overpotential curves show the same C : H R_p ratios of ~30, 5 and 2 for the model Ni/YSZ, model Ni/YSZ-HCP, and porous Ni–SZ electrodes, respectively (Fig. 2). For the two model electrodes, the ratio increases with anodic polarization and decreases with cathodic polarization to about double and half, respectively, at ±0.2 V compared with the value near open-circuit. However, the ratio for the porous electrode remains nearly constant in the range of 1.5 to 2. All three electrodes have considerably faster anodic than cathodic kinetics, with the largest difference for the model Ni/

Table 1 Summary of the EIS results for all of the electrodes tested

					R_p			
Electrode abbreviation	Materials|electrolyte	Geometry	Rxn. site	T [°C]	Units	H_2/H_2O	CO/CO_2	Ratio
Ni/SZ ME	Ni|YSZ	Model	3PB	1000	kΩ	3.68	125	34.0
Ni/SZ ME	Ni|YSZ	Model	3PB	850	kΩ	20.8	701	33.7
Ni/SZ ME	Ni|YSZ	Model	3PB	750	kΩ	98.0	2860	29.2
Ni/SZ-HCP ME	Ni|YSZ	Model	3PB	860	kΩ	1.41	5.90	4.18
Ni/SZ-redox ME	Ni|YSZ	Model	3PB	850	kΩ	7.55	25.8	3.42
Ni–SZ-supported PE	Ni-YSZ|YSZ	Porous	3PB	750	Ω cm^2	0.099	0.20	1.97
Ni–SZ PE	Ni-ScYSZ|ScYSZ	Porous	3PB	850	Ω cm^2	0.067	0.14	2.01
CGOn/STN ME	CGOn/STN|YSZ	Model	2PB	850	MΩ	2.50	0.40	0.16
CGOn/STN PE	CGOn/STN|YSZ	Porous	2PB	800	Ω cm^2	0.31	0.49	1.59
CGOn/STN-redox PE	CGOn/STN|YSZ	Porous	2PB	800	Ω cm^2	0.12	0.66	5.68
CGOn-2.5 μm PE	CGOn|YSZ	Porous	2PB	800	Ω cm^2	0.010	0.076	7.93
CGO-SS-10 μm PE	CGO|ScYSZ	Porous	2PB	800	Ω cm^2	0.066	0.17	2.59
CGO-SS-18 μm PE	CGO|YSZ	Porous	2PB	750	Ω cm^2	0.078	0.21	2.69
CGO-inhomog-30 μm PE	CGO|YSZ	Porous	2PB	750	Ω cm^2	0.43	0.67	1.55
CGO-SS-18 μm-Au PE	CGO|YSZ	Porous	2PB	750	Ω cm^2	1.35	0.86	0.64

ART ■ C5FD00048C

SZ (factors of 26 and 4.1 higher current at ±0.2 V for H_2/H_2O and CO/CO_2, respectively), a smaller difference for the model Ni/SZ-HCP (factors of 4.0 and 1.2), and the smallest difference for the porous Ni–SZ electrode (factors of 2.1 and 1.5). For these 3 cells, the ohmic resistance, and corresponding heating during DC measurements, is minimal due to the cell geometries, as the current spreads outwards from the small working electrode into the large electrolyte pellet to the large counter electrode.

Mechanisms

One might consider that the higher activity in H_2/H_2O than CO/CO_2 has the same explanation as the higher activity in anodic than cathodic polarization. Indeed, gas diffusion has been shown to be partly responsible for both effects in the case of the Ni–YSZ composites with a thick porous support layer,[25] but here the largest gas composition difference and anodic/cathodic asymmetry is observed for the model electrodes which have negligible gas diffusion resistance.

We propose that impurities and the 3D microstructure are responsible for the decreasing difference in activity in H_2/H_2O *vs.* CO/CO_2 in the progression from the model electrode to the model electrode with HCP to the porous electrode. It is well established that in Ni/SZ model electrodes, the 3PB is blocked by glassy impurity phases that segregate from the raw materials,[14] unless extremely pure raw materials were used in preparation of the cell,[38,23] which was not the case here. The large activation of Ni/SZ during HCP treatment has been reported to result from nano-structuring of the 3PB which occurs when YSZ is partially reduced and interacts with Ni during HCP treatment[45,46] and/or from reduction and mobilization of impurities that were accumulated at the 3PB.[42] Both effects would lead to a fresh 3PB with a lower concentration of impurities. In this case, microscopy revealed that the brief treatment rearranged the Ni/YSZ interface and a new, considerably longer 3PB was formed. No analysis of impurities has been carried out. We observed that subjecting the model Ni/SZ electrodes to a redox cycle (oxidizing to NiO and then reducing again), which also rearranges the 3PB,[30] led to a similar decrease in the C : H R_p ratio down to 3.4 (see Table 1). We focus on the HCP results here because current–overpotential curves were not measured after the redox cycle. The segregated impurities apparently inhibit the CO/CO_2 reaction more so than the H_2/H_2O reaction, as formation of a fresh 3PB decreases the C : H R_p ratio by nearly an order of magnitude. This might be because H_2/H_2O related species are transported more rapidly through or on the surface of the impurity phases or maybe partly through the Ni.[47] The especially large activation for the Ni/SZ model electrode in anodic polarization in H_2/H_2O (Fig. 2a and b), which generates H_2O at the 3PB, might be due to the same effect and/or due to a temporary rearrangement of the impurities by their reaction with H_2O, *e.g.* vaporization of SiO_2 by forming the hydroxide, and subsequent re-deposition at the 3PB.[48,49] The well-known anodic activation by 3PB pH_2O dependence, exothermicity of the anodic electrochemical reaction (and cathodic endothermicity), and possibly enhanced kinetics of the actual charge-transfer reaction in anodic polarization[25,50] cannot account for the factor of 26 higher current at +0.2 V *vs.* −0.2 V overpotential in H_2/H_2O. Regardless of the impurity content and the exact value of the C : H R_p ratio, the consistently observed higher activity for the H_2/H_2O *vs.* CO/CO_2 reactions at Ni/SZ may be due to the high mobility of H

ART ■ C5FD00048C

on Ni,[51] or it could simply be due to a more beneficial energetic landscape for the overall reaction scheme.

The 3PB of the model Ni/SZ electrodes has a high impurity content due to the relatively large volumes of Ni and YSZ compared with the 3PB reaction zone. The Ni and YSZ components act as large reservoirs of impurities. Therefore, the fresh 3PB of the model Ni/SZ-HCP electrode should more closely match the 3PBs found in porous electrodes. However, the C : H R_p ratio decreases from 4–5 for the model Ni/SZ-HCP electrode to 2 for the porous Ni–SZ electrode. This difference can be explained by the 3D microstructure of the porous composite electrode, which extends the ER zone into the electrode thickness due to the ionic conductivity in the electrode. The lower CO/CO_2 reaction rate leads to extension of the reaction zone farther into the electrode, which partly compensates for the lower 3PB reaction rate. This effect is illustrated in Fig. 4a, which shows modelling results of the total porous electrode R_p *vs.* electrode thickness for two different ER rates that differ by a factor of 4 – the approximate C : H R_p ratio for the model Ni/SZ-HCP electrode. As the electrode becomes thick enough, the R_p ratio decreases to a

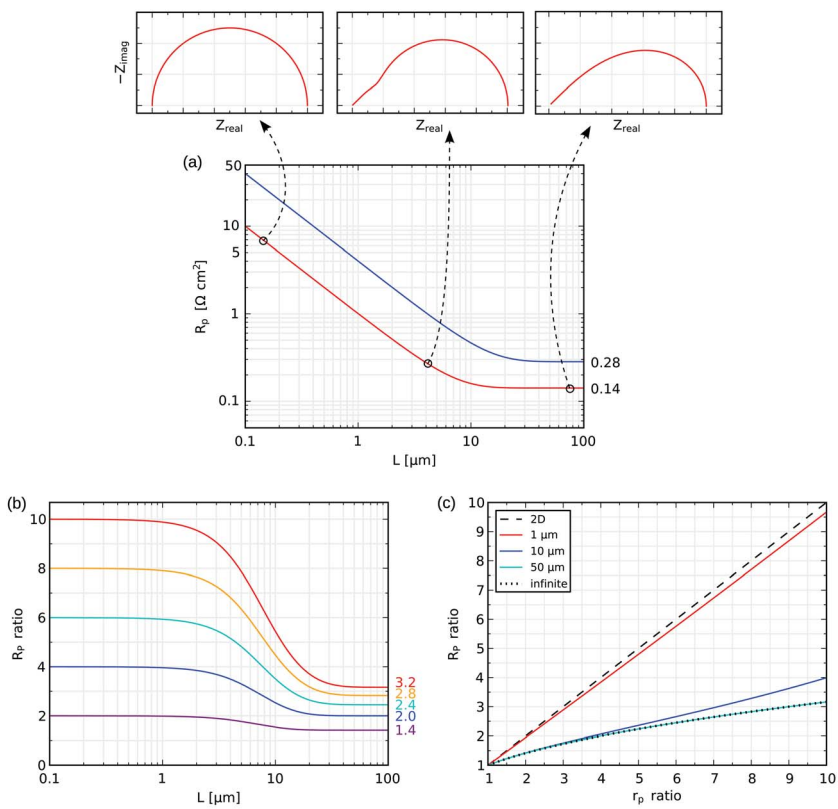

Fig. 4 Porous electrode modelling, showing the total electrode R_p as a function of electrode thickness L and ER site r_p. (a) Electrode R_p *vs.* thickness for 2 different r_p values that have a ratio of 4. (b) Electrode R_p ratio *vs.* thickness for 5 different r_p ratios. (c) Electrode R_p ratio *vs.* r_p ratio for 5 different electrode thickness values.

ART ■ C5FD00048C

factor of 2, in close agreement with the experimental results for the porous Ni–SZ electrode.

The porous electrode model is a 1-D transmission line model that represents the porous electrode as a continuum of ER resistances coupled with ionic and electronic currents which extend through the electrode thickness, away from the electrolyte and towards it, respectively:

$$R_p = \sqrt{r_p r_i}\,\coth\left(L\sqrt{\frac{r_p}{r_i}}\right)$$

where R_p is the total porous electrode polarization resistance, r_p is the polarization resistance of the ER sites (Ω cm), r_i is the ionic transport resistance (Ω cm^{-1}), and L is the electrode thickness (cm). This general analytical model has been shown to successfully describe the impedance of the porous SOC composite and mixed-conducting electrodes that are macroscopically homogeneous.[43,44] It is valid for low current (near open-circuit) and neglects gradients in gas composition, temperature, *etc.*

For 3PB-based electrodes, r_p is the 3PB length-specific polarization resistance (LSR_p) divided by the 3PB density (3PB length per electrode volume). Realistic values of 4 kΩ cm for LSR_p and 3 μm μm^{-3} for the 3PB density were used for the modelling results. Changing the ionic resistivity r_i does not change the R_p ratios; it only changes the thickness value at which the minimum porous electrode R_p is reached and the value of that minimum R_p value. A realistic r_i value of 200 Ω cm was used for these simulations, which corresponds to an effective ionic conductivity of 0.005 S cm^{-1} in the composite electrode, *e.g.* a bulk conductivity of 0.04 S cm^{-1}, an ionic phase volume fraction of 0.3, and a tortuosity factor of 2.5. The real values of these parameters and the 3PB parameters differ considerably for actual porous electrodes fabricated using different procedures. These assumptions are simply the right order of magnitude and they are sufficient for illustrating the C : H R_p ratios because they have no impact on the ratios.

Fig. 4b shows the modelling results expressed as ratios (the line beginning with an R_p ratio of 4 is the ratio of the two lines shown in Fig. 4a). This shows that a larger difference in r_p is compensated more by the porous composite electrode structure, with an r_p ratio of 10 leading to an R_p ratio of only 3.2, and a smaller difference is compensated less, with an r_p ratio of 2 resulting in an R_p ratio of 1.4. Finally, Fig. 4c shows the R_p ratio *vs.* the r_p ratio at different electrode thickness values, including ~zero thickness (the 2D model electrode situation) and infinite thickness (the usual 3D porous electrode situation).

Doped ceria 2PB-based electrodes

In contrast to Ni/SZ and other 3PB-based electrodes, the entire gas-exposed surface of ceria and other MIEC materials is in principle active for electrochemical reactions. One issue with ceria, however, is that its electronic conductivity is low, which leads to non-negligible ohmic losses in porous electrodes comprised only of doped ceria unless the electrode is extremely thin and has low porosity and tortuosity. Ceria based electrodes are usually composites with a better electron conductor. The conventional method of forming a composite is by mixing particles and sintering, leading to a random structure. An alternative way is by coating the ceria onto an electronic backbone, which both ensures better

percolation of the two phases and enables low temperature processing of the ceria, maintaining the ceria as nanoparticles. We use the coating approach here, with STN as the electronic conducting phase.

Similar to the Ni/SZ experiments, several different types of CGO-based electrodes were characterized to study the influence of nano/microstructure (illustrated in Fig. 1). The first set of electrodes employed STN as the electronic conducting backbone. The second set of electrodes included no additional electronic current collector in the porous structure, depending only on porous Pt or Au (by sintering the respective pastes) on top.

Electrodes with STN electron-conducting backbone:

1. CGO nanoparticles placed at the 2D interface of the electronic conductor STN pressed down onto a polished YSZ surface (hereafter referred to as the "CGOn/STN model electrode") – as well as the same type of electrode without the CGOn, *e.g.* only the STN/SZ interface, for comparison.

2. CGO nanoparticles coating the surfaces inside a 3D porous STN backbone ("CGOn-STN porous electrode").

3. The same type of electrode as #2, after a redox cycle ("CGOn-STN-redox porous electrode").

Electrodes comprised solely of doped ceria:

1. A 2.5 μm thick porous electrode comprised of CGO nanoparticles, prepared by spin-coating and sintering at 800 °C ("CGOn-2.5 μm porous electrode").

2. A 10 μm thick porous electrode comprised of larger (200–400 nm) particles, prepared by slurry spraying and sintering at 1200 °C ("CGO-SS-10 μm porous electrode").

3. A 30 μm thick porous electrode comprised of 200–400 nm size particles with a highly inhomogeneous, regionally agglomerated microstructure, prepared by screen-printing and sintering at 1200 °C ("CGO-inhomog-30 μm porous electrode").

4. An 18 μm thick porous electrode similar to #2, only thicker ("CGO-SS-18 μm porous electrode").

5. The same type of electrode as #4, but with a porous Au current collector layer (prepared by sintering Au paste; "CGO-SS-18 μm-Au porous electrode") rather than porous Pt as used for the other ceria-based porous electrodes.

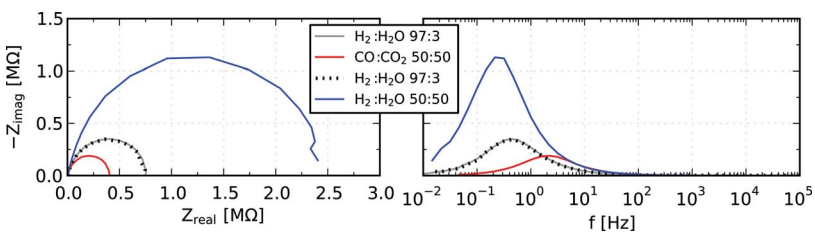

Fig. 5 EIS measured on a CGOn/STN model electrode at 850 °C in 3 different gas compositions.

ART ■ C5FD00048C

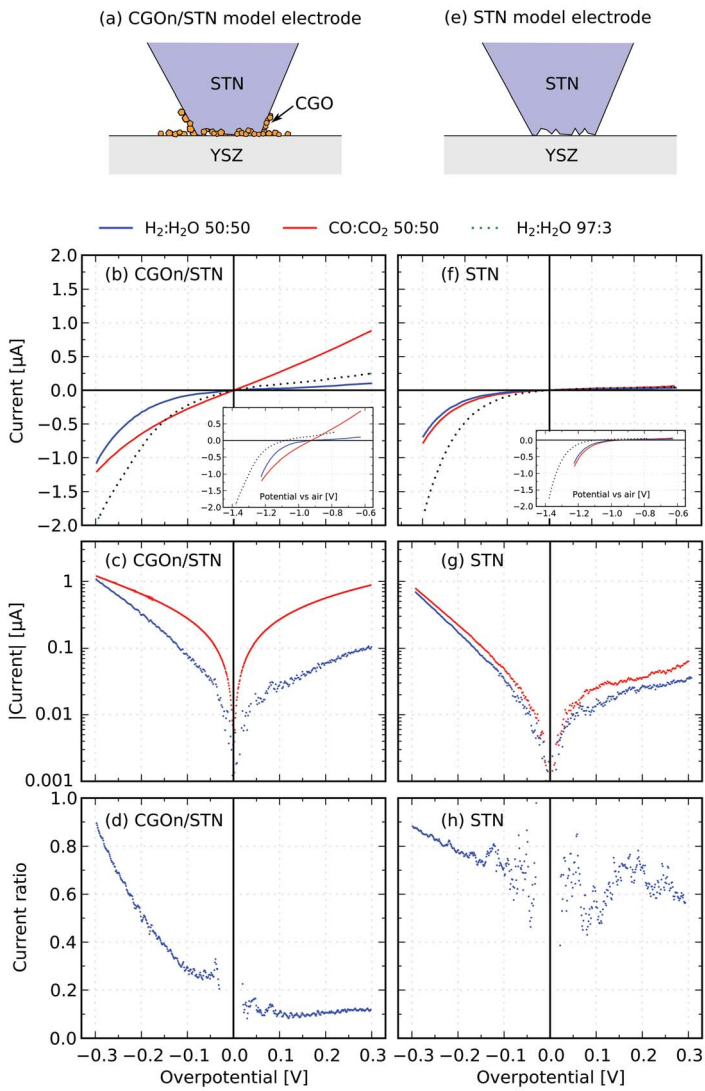

Fig. 6 Current–overpotential curves measured on CGOn/STN (b–d) and STN (f–h) model electrodes. The electrode configurations are illustrated in (a) and (b). Current ratio (d and h) is the ratio of the current measured in H_2/H_2O to that measured in CO/CO_2.

Model electrodes

EIS and current–overpotential curves measured on the CGOn/STN model electrode are shown in Fig. 5 and 6, respectively. The electrode configuration is illustrated in Fig. 6a.

The most remarkable observation about the impedance of this electrode is that the activity in CO/CO_2 is much higher than in H_2/H_2O; the C : H R_p ratio is 0.16 (Fig. 5). This behaviour is opposite to that of the Ni/SZ electrodes discussed earlier. Although ceria is well known as a catalyst for CO/CO_2 reactions

ART ■ C5FD00048C

(considering that it is used as an active catalyst support for 3-way CO oxidation catalysts that treat automotive exhaust, as well as for the water gas shift reaction and preferential oxidation of CO), we are not aware of any previous reports in the literature that show ceria is an excellent CO/CO_2 electrocatalyst, which exhibits higher activity for CO/CO_2 than for H_2/H_2O electrochemical reactions.

The electrode activity was stable throughout the measurement sequence, as can be seen in the EIS measurements in $pH_2/pH_2O = 0.97/0.03$ atm during the sequence (Fig. 5). At low current, the current–overpotential curves show the same relative activity (Fig. 6d). A major difference in the shapes of the current–overpotential curves can be observed for the H_2/H_2O and CO/CO_2 reactions – the CO/CO_2 curve is nearly linear, whereas the H_2/H_2O curve shows tremendous cathodic activation. The cathodic activation is so strong that the H_2O electrolysis current approximately "catches up" to the CO_2 electrolysis current at -0.3 V overpotential. Higher activity in H_2O electrolysis than in H_2 oxidation has been observed on various ceria electrodes and interpreted as being due to the increased surface reduction of ceria.[52–54] This observation is consistent with the reported increase in oxygen surface exchange rate with decreasing pO_2.[55–57] Only very slight cathodic activation is present in CO_2 electrolysis. The higher activity for the electrochemical reduction of H_2O and CO_2 than for oxidation of H_2 and CO is another example of opposite behaviour to the Ni/SZ electrodes.

We propose that a higher surface concentration of reaction sites on the ceria nanoparticles in CO/CO_2 than in H_2/H_2O underlies the higher activity. The nature of the rate limiting reaction step on Sm-doped ceria surfaces in H_2/H_2O and CO/CO_2 has been recently suggested to relate to electron transfer between Ce^{3+} and surface OH^- and CO_3^{2-} respectively (speculated to be so at ambient pressure).[27,28] DFT modelling has shown that the ceria surface is more easily reduced by CO than by H_2.[58] Surface reduction leads to increased surface concentrations of oxygen vacancies and polarons (Ce^{3+}), which directly or indirectly provide ER sites.

The impedance data supports this explanation. All of the impedance measurements appear as single near-perfect semicircles in the complex plane. The measurements in $pH_2/pH_2O = 0.5/0.5$ atm and $pH_2/pH_2O = 0.97/0.03$ atm show a similar summit frequency (f_s) of 0.3–0.4 Hz, whereas the measurement in $pCO/pCO_2 = 0.5/0.5$ atm shows a considerably higher f_s value of 2.1. The summit frequency relates to the resistance R and capacitance C by $f_s = 1/(2\pi RC)$. For doped ceria and other mixed conductors, the capacitance is dominated by bulk chemical capacitance.[26,59,60] The chemical capacitance results from the presence of mixed valence Ce^{3+}/Ce^{4+} and increases with decreasing pO_2, within the pO_2 range explored here. The resistance is dominated by the 2PB ER resistance at the ceria|gas interface.[60,16] In the two H_2/H_2O environments, the unchanged summit frequency means the product of R and C is unchanged – in the more reducing H_2/H_2O environment, the reduction of the bulk ceria increases the chemical capacitance and the reduction of surface ceria decreases the surface reaction resistance. However, the $pH_2/pH_2O = 0.5/0.5$ atm and $pCO/pCO_2 = 0.5/0.5$ atm environments yield almost the same pO_2 (5.3×10^{18} and 6.1×10^{18} atm respectively) at the measurement temperature of 850 °C, so the chemical capacitance is the same in both environments. Yet the R_p has clearly decreased (causing the increase in f_s), suggesting that the ceria surface is more reduced (or provides a higher ER rate by another mechanism) in CO/CO_2 compared to H_2/H_2O when both environments provide the same pO_2.

The nearly linear current–overpotential curve in CO/CO_2 might be due to the presence of a high concentration of reactive surface species that is essentially independent of polarization and corresponding oxygen activity.

The higher activity in cathodic *vs.* anodic polarization can be similarly explained by reduction of the oxides during cathodic polarization, leading to enhanced surface concentration of reaction sites. This is not a special feature of ceria or nanoceria, evidenced by the similar current–overpotential behaviour of the STN model electrode without the ceria nanoparticles measured during the same test sequence (Fig. 6f and g). Cathodic activation has also been observed previously in the literature on oxide electrodes comprised of STN,[61] Sm-doped ceria,[27] a composite of CGO and La-doped $SrTiO_3$,[62] and various molybdenum oxide containing perovskites.[34]

Three important questions that arise are (i) whether the unique behaviour observed with the model electrodes can translate to a technologically relevant porous electrode, (ii) whether the high activity for CO/CO_2 reactions is specific to nanoparticulate ceria, and (iii) the possible role of the STN support. Here we briefly explore these considerations.

Porous electrodes

EIS measured on the CGOn/STN porous electrodes, which are comprised of the same materials (CGO nanoparticles on STN backbones) as the model electrodes, did not show a C : H R_p ratio far below 1 (Fig. 7), as was observed for the model electrodes. One CGO-infiltrated STN electrode exhibited a ratio of 1.6 (Fig. 7a) – still a lower value than observed for any of the Ni/SZ electrodes. The same type of electrode was subjected to a redox cycle, which causes a decrease in R_p, possibly due to formation of nano-sized cracks in the CGO coating, thereby re-gaining nanostructured features that were lost during particle coarsening.[30] The C : H R_p ratio increased to 5.7 (Fig. 7b). These two electrodes exhibit typical Gerischer-like porous electrode impedance, similar to the porous Ni–SZ electrodes. The presence of the Gerischer-like shapes is expected because the ionic conductivity is low in these electrodes, as it is provided only by the thin coatings of CGO

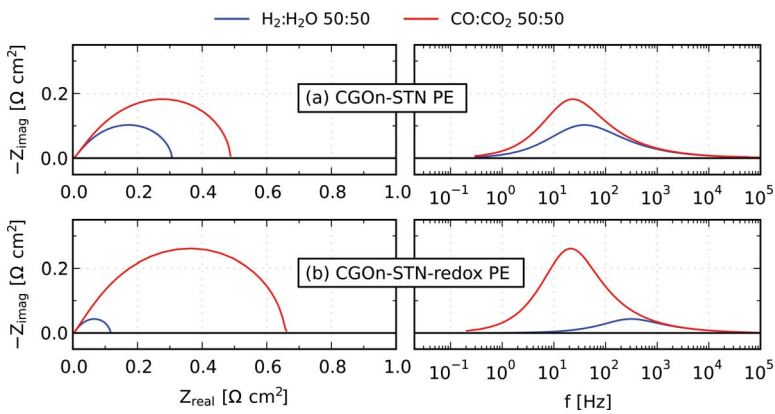

Fig. 7 EIS measured on porous electrodes with CGO nanoparticles coated on STN backbones in 50 : 50 mixtures of H_2/H_2O and CO/CO_2 at 800 °C.

ART ■ C5FD00048C

nanoparticles, and therefore the ER zone is not expected to extend to the full 20 μm electrode thickness.

Electrodes made of only CGO were also studied (Fig. 8). A thin nano-structured electrode (CGOn-2.5 μm porous electrode) exhibited an exceptionally high activity ($R_p = 0.01\ \Omega\ cm^2$ in H_2/H_2O, including SGL diffusion). However the C : H R_p ratio was high at 6.9 (Fig. 8a). For a thicker electrode made of larger 200–400 nm sized particles (CGO-SS-10 μm porous electrode), the C : H R_p ratio was 2.6 (Fig. 8b). For a yet thicker electrode, which also had an inhomogeneous microstructure due to particle agglomeration during fabrication (CGO-inhomog-30 μm porous electrode), the ratio was 1.6 (Fig. 8c). Another thick electrode (CGO-SS-18 μm porous electrode) showed a ratio of 2.7. Finally, the same type of 18 μm thick electrode tested with Au paste as the current collector was the only one to show an inverse ratio of 0.6 — higher activity for CO/CO_2 than for H_2/H_2O, as observed for the model electrode. It should be noted that the impedance was relatively large for this last electrode, as well as the cell ohmic resistance which was more than double the ohmic resistance of the same type of cell with Pt paste (CGO-SS-18 μm porous electrode), indicating a poor coating of the Au paste. Therefore, the area-

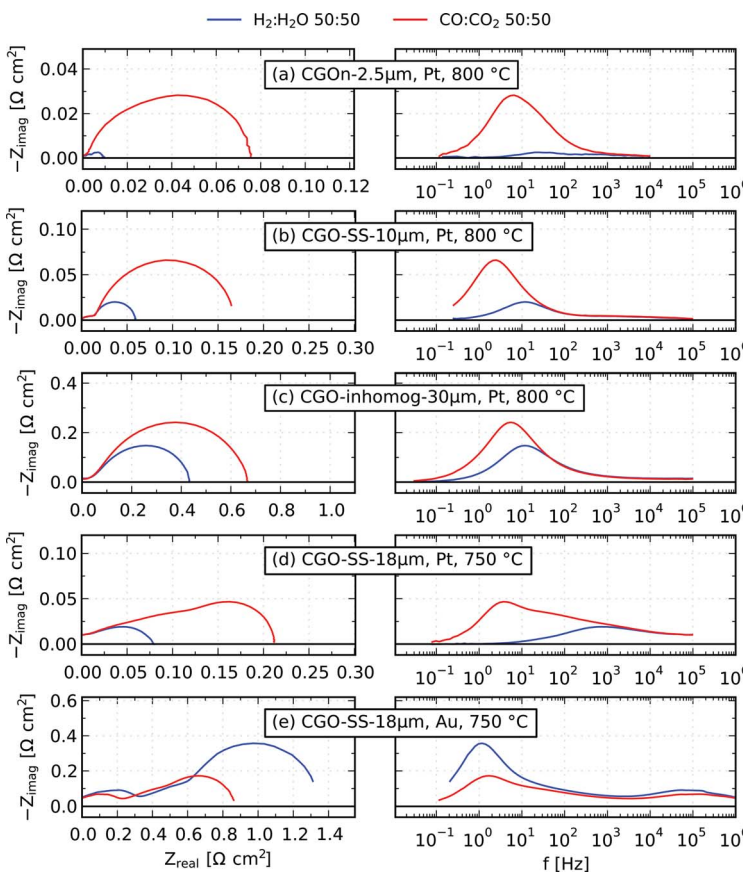

Fig. 8 EIS measured on various porous CGO electrodes with either Pt or Au paste used for electronic current collection, in 50 : 50 mixtures of H_2/H_2O and CO/CO_2.

ART ■ C5FD00048C

normalized impedance of the electrode with Au paste, which is calculated with the assumption of even current collection across the cell area, should not be compared with that measured on the Pt paste cell. The impedance response of these CGO electrodes varied from a somewhat skewed semicircle for thinner electrodes to a Gerischer-like porous electrode response for thicker electrodes, which indicates that the ER zone extends to a thickness of between 10–18 μm s at these test conditions. As the ionic conductivity is much higher in these electrodes due to the larger volume fraction of the ion conductor, CGO, than in the case of CGO-infiltrated STN, the ER zone extends farther into the thickness, assuming the same surface reaction rates. Table 1 gives a summary of the EIS results for all of the model and porous ceria-based electrodes.

The relatively high C : H R_p ratios for the nanostructured electrodes might be due to gas diffusion limitations in the porous structures. In the case of the CGOn-STN porous electrode, the nano-cracks may provide additional surface area that is only accessible to the smaller H_2/H_2O molecules, providing no additional reaction sites for CO/CO_2. Similarly, the CGOn-2.5 μm porous electrode has nano-pores which may not be accessible. Furthermore, Knudsen diffusion is present in such electrodes.[37]

The relatively low C : H R_p ratios for thicker electrodes might relate to the porous electrode thickness effect described earlier (Fig. 4). However, another possibility is that in the thinner electrodes the ER zone extends to the end of the electrode thickness, thereby reaching the CGO/Pt/gas interface at the current collector, which may provide enhanced activity. Sintered Pt paste consists of large particles and by itself shows extremely low activity ($R_p > 100\ \Omega\ cm^2$ for porous Pt when applied directly to the electrolyte), but the nanostructured CGO provides a high density of interfaces in contact with the Pt particles. The data measured with Au paste indicates that the CGO/Pt/gas interface may indeed be responsible for improving the electrode kinetics, especially in H_2/H_2O compared with CO/CO_2. Au is a poor electrocatalyst for H_2/H_2O as compared to Pt,[63] and therefore the CGO/Au/gas interface does not promote the measured electrode kinetics substantially. Also, the results obtained with Au paste show that STN is not needed to obtain the higher activity of CGO in CO/CO_2 than in H_2/H_2O. Nevertheless, the role of the Au paste in establishing this relation remains to be investigated. Furthermore, the electrode did not contain nanoparticles (it was a sintered structure with 200–400 nm size particles), suggesting that nanoparticles are not needed. Further testing without the Pt current collector would be worthwhile to confirm these findings.

Conclusions

The electrode kinetics of the H_2/H_2O and CO/CO_2 reactions were investigated for Ni/SZ, CGO, and CGOn/STN in model electrode and porous electrode geometries and with different micro/nanostructures. The ratio of electrode R_p in CO/CO_2 *vs.* H_2/H_2O was found to decrease from 33 to 2 when comparing model Ni/SZ and porous Ni–SZ electrodes. Experimental evidence and modelling suggested that a greater concentration of impurities at the 3PB in the model electrode lead to a higher ratio, and the nature of the porous electrode reaction zone extension into electrode thickness leads to a decreased ratio. Based on the analysis, the ratio for the actual 3PBs in the porous electrode is expected to be around 4.

ART ■ C5FD00048C

Besides showing higher activity for H_2/H_2O reactions than CO/CO_2 reactions, the Ni/SZ interface is more active for oxidation than reduction. On the other hand, we found that CGOn/STN model electrodes show the opposite behaviour in both cases – higher activity for CO/CO_2 and higher activity for reduction, *e.g.* the highest current could be obtained for CO_2 electrolysis. To the best of our knowledge, this is the first report of a higher electrocatalytic activity for CO/CO_2 than for H_2/H_2O reactions on CGO nanoparticles in the absence of gas diffusion limitations. We proposed that enhanced surface reduction of the doped ceria in CO/CO_2, at the same pO_2, underlies this behaviour. This effect could not be observed in CGO based porous electrodes, except in one case where Au instead of Pt was used as the electronic current collector, suggesting that the CGO/Pt interfaces may be selectively enhancing the activity of the H_2/H_2O reaction for those porous electrodes. Greater gas diffusion limitations for CO/CO_2 than for H_2/H_2O, especially with nanostructured features involved, is another possible explanation for the different relative activities of the porous electrodes and the model electrodes in CO/CO_2 and H_2/H_2O.

Acknowledgements

We would like to thank Peter Blennow for valuable discussions; Tânia Ramos for providing Ni–YSZ symmetrical cells; Bhaskar Reddy Sudireddy, Theis Løye Skafte, Jean-Claude Njodzefon, Vahid Vakili, Lene Knudsen, Annelise Mikkelsen and other colleagues and laboratory staff at DTU Energy for assistance with sample fabrication and experiments. We gratefully acknowledge financial support from Energinet.dk through the ForskEL programme "Solid Oxide Fuel Cells for the Renewable Energy Transition" contract no 2014-1-12231 and from the Program Commission on Sustainable Energy and Environment, The Danish Council for Strategic Research, via the SERC project (http://www.serc.dk), contract no. 2104-06-0011.

References

1 S. H. Jensen, P. H. Larsen and M. Mogensen, *Int. J. Hydrogen Energy*, 2007, **32**, 3253–3257.
2 N. Q. Minh and M. B. Mogensen, *Electrochem. Soc. Interface*, 2013, 55.
3 C. Graves, S. D. Ebbesen, M. Mogensen and K. S. Lackner, *Renewable Sustainable Energy Rev.*, 2011, **15**, 1–23.
4 C. Graves, S. D. Ebbesen, S. H. Jensen, S. B. Simonsen and M. B. Mogensen, *Nat. Mater.*, 2015, **14**, 239–244.
5 D. M. Bierschenk, J. R. Wilson and S. A. Barnett, *Energy Environ. Sci.*, 2011, **4**, 944–951.
6 S. D. Ebbesen and M. Mogensen, *J. Power Sources*, 2009, **193**, 349–358.
7 Z. Zhan and S. A. Barnett, *Science*, 2005, **308**, 844–847.
8 C. Graves, S. D. Ebbesen and M. Mogensen, *Solid State Ionics*, 2011, **192**, 398–403.
9 R. Knibbe, A. Hauch, J. Hjelm, S. D. Ebbesen and M. Mogensen, *Green*, 2011, **1**, 141–169.
10 A. Weber, in *Encyclopedia of Electrochemical Power Sources*, Elsevier, Amsterdam, 2009, pp. 120–134.

11 M. Chen, Y.-L. Liu, J. J. Bentzen, W. Zhang, X. Sun, A. Hauch, Y. Tao, J. R. Bowen and P. V. Hendriksen, *J. Electrochem. Soc.*, 2013, **160**, F883–F891.
12 A. Hauch, A. Hagen, J. Hjelm and T. Ramos, *J. Electrochem. Soc.*, 2014, **161**, F734–F743.
13 S. D. Ebbesen, C. Graves, A. Hauch, S. H. Jensen and M. Mogensen, *J. Electrochem. Soc.*, 2010, **157**, B1419–B1429.
14 M. Mogensen and K. V. Hansen, in *Handbook of Fuel Cells*, John Wiley & Sons, Ltd, 2010.
15 J. B. Goodenough and Y.-H. Huang, *J. Power Sources*, 2007, **173**, 1–10.
16 W. C. Chueh and S. M. Haile, *Annu. Rev. Chem. Biomol. Eng.*, 2011.
17 M. Mogensen, N. M. Sammes and G. A. Tompsett, *Solid State Ionics*, 2000, **129**, 63–94.
18 C. Chatzichristodoulou, P. T. Blennow, M. Søgaard, P. V. Hendriksen and M. B. Mogensen, in *Catalysis by Ceria and Related Materials*, Imperial College Press, 2013, vol. 12, pp. 623–782.
19 W. C. Chueh, Y. Hao, W. Jung and S. M. Haile, *Nat. Mater.*, 2012, **11**, 155–161.
20 W. Jung, J. O. Dereux, W. Chueh, Y. Hao and S. M. Haile, *Energy Environ. Sci.*, 2012.
21 M. Mogensen, J. Høgh, K. V. Hansen and T. Jacobsen, *ECS Trans.*, 2007, **7**, 1329–1338.
22 V. Yurkiv, A. Utz, A. Weber, E. Ivers-Tiffée, H.-R. Volpp and W. G. Bessler, *Electrochim. Acta*, 2012, **59**, 573–580.
23 A. Utz, A. Leonide, A. Weber and E. Ivers-Tiffée, *J. Power Sources*, 2011, **196**, 7217–7224.
24 W. G. Bessler, M. Vogler, H. Störmer, D. Gerthsen, A. Utz, A. Weber and E. Ivers-Tiffée, *Phys. Chem. Chem. Phys.*, 2010, **12**, 13888.
25 J.-C. Njodzefon, D. Klotz, A. Kromp, A. Weber and E. Ivers-Tiffée, *J. Electrochem. Soc.*, 2013, **160**, F313–F323.
26 R. D. Green, C.-C. Liu and S. B. Adler, *Solid State Ionics*, 2008, **179**, 647–660.
27 Z. A. Feng, M. L. Machala and W. C. Chueh, *Phys. Chem. Chem. Phys.*, 2015.
28 Z. A. Feng, F. El Gabaly, X. Ye, Z.-X. Shen and W. C. Chueh, *Nat. Commun.*, 2014, **5**.
29 C. R. Graves, S. D. Ebbesen and M. Mogensen, *ECS Trans.*, 2009, **25**, 1945–1955.
30 C. Graves, *ECS Trans.*, 2013, **57**, 3127–3136.
31 T. Ramos, K. Thydén and M. Mogensen, *ECS Trans.*, 2010, **28**, 123–139.
32 T. Ramos, M. Søgaard and M. B. Mogensen, *J. Electrochem. Soc.*, 2014, **161**, F434–F444.
33 P. Blennow, K. K. Hansen, L. R. Wallenberg and M. Mogensen, *ECS Trans.*, 2008, **13**, 181–194.
34 C. Graves, B. R. Sudireddy and M. Mogensen, *ECS Trans.*, 2010, **28**, 173–192.
35 A. Samson, M. Søgaard, R. Knibbe and N. Bonanos, *J. Electrochem. Soc.*, 2011, **158**, B650–B659.
36 S. Primdahl and M. Mogensen, *J. Electrochem. Soc.*, 1999, **146**, 2827–2833.
37 A. M. Hussain, J. V. T. Høgh, T. Jacobsen and N. Bonanos, *Int. J. Hydrogen Energy*, 2012, **37**, 4309–4318.
38 A. Utz, H. Stormer, A. Leonide, A. Weber and E. Ivers-Tiffee, *J. Electrochem. Soc.*, 2010, **157**, B920–B930.
39 C. Graves, *RAVDAV data analysis software, version 0.9.8*, 2014.

ART ■ C5FD00048C

40 M. S. Schmidt, K. V. Hansen, K. Norrman and M. Mogensen, *Solid State Ionics*, 2008, **179**, 2290–2298.
41 M. S. Schmidt, K. V. Hansen, K. Norrman and M. Mogensen, *Solid State Ionics*, 2008, **179**, 1436–1441.
42 J. Høgh, K. V. Hansen, K. Norrman, I. Chorkendorff, T. Jacobsen and M. Mogensen, *Solid State Ionics*, 2013, **234**, 11–18.
43 V. Sonn, A. Leonide and E. Ivers-Tiffee, *J. Electrochem. Soc.*, 2008, **155**, B675–B679.
44 J. Nielsen and J. Hjelm, *Electrochim. Acta*, 2014, **115**, 31–45.
45 D. Klotz, B. Butz, A. Leonide, J. Hayd, D. Gerthsen and E. Ivers-Tiffee, *J. Electrochem. Soc.*, 2011, **158**, B587–B595.
46 D. Klotz, J. Szasz, A. Weber and E. Ivers-Tiffée, *ECS Trans.*, 2012, **45**, 241–249.
47 K. V. Jensen, R. Wallenberg, I. Chorkendorff and M. Mogensen, *Solid State Ionics*, 2003, **160**, 27–37.
48 M. S. Schmidt, K. Vels Hansen, K. Norrman and M. Mogensen, *Solid State Ionics*, 2009, **180**, 431–438.
49 A. Hauch, S. D. Ebbesen, S. H. Jensen and M. Mogensen, *J. Electrochem. Soc.*, 2008, **155**, B1184–B1193.
50 S. D. Ebbesen and M. Mogensen, *ECS Trans.*, 2013, **50**, 167–182.
51 M. Mogensen and S. Skaarup, *Solid State Ionics*, 1996, **86–88**(2), 1151–1160.
52 C. Zhang, M. E. Grass, A. H. McDaniel, S. C. DeCaluwe, F. E. Gabaly, Z. Liu, K. F. McCarty, R. L. Farrow, M. A. Linne, Z. Hussain, G. S. Jackson, H. Bluhm and B. W. Eichhorn, *Nat. Mater.*, 2010, **9**, 944–949.
53 L. Wang, C. Zhang, M. Grass, Y. Yu, K. Gaskell, Z. Hussain, Z. Liu, B. Eichhorn and G. Jackson, *ECS Trans.*, 2011, 1435–1444.
54 S. C. DeCaluwe and G. Jackson, *ECS Trans.*, 2011, **35**, 2883–2895.
55 A. Karthikeyan and S. Ramanathan, *Appl. Phys. Lett.*, 2008, **92**, 243109–243109.
56 T. Horita, K. Yamaji, N. Sakai, M. Ishikawa, H. Yokokawa, T. Kawada, and M. Dokiya, *Electrochem. Solid-State Lett.*, 1998, **1**, 4–6.
57 M. Katsuki, S. Wang, K. Yasumoto, and M. Dokiya, *Solid State Ionics*, 2002, **154–155**, 589–595.
58 D. Knapp and T. Ziegler, *J. Phys. Chem. C*, 2008, **112**, 17311–17318.
59 S. B. Adler, J. A. Lane and B. C. H. Steele, *J. Electrochem. Soc.*, 1996, **143**, 3554–3564.
60 W. C. Chueh, W. Lai and S. M. Haile, *Solid State Ionics*, 2008, **179**, 1036–1041.
61 P. Blennow, K. K. Hansen, L. R. Wallenberg and M. Mogensen, *Solid State Ionics*, 2009, **180**, 63–70.
62 O. A. Marina, L. R. Pederson, M. C. Williams, G. W. Coffey, K. D. Meinhardt, C. D. Nguyen and E. C. Thomsen, *J. Electrochem. Soc.*, 2007, **154**, B452–B459.
63 R. Baker, J. Guindet and M. Kleitz, *J. Electrochem. Soc.*, 1997, **144**, 2427–2432.

ART ■ C5FD00048C